Construction of a multi-scale spiking model of macaque visual cortex

Maximilian Schmidt[1], Rembrandt Bakker[1,2], Markus Diesmann[1,3,4] and Sacha J. van Albada[1]

[1]Institute of Neuroscience and Medicine (INM-6) and Institute for Advanced Simulation (IAS-6) and JARA BRAIN Institute I, Jülich Research Centre, Jülich, Germany

[2]Donders Institute for Brain, Cognition and Behavior, Radboud University Nijmegen, Netherlands

[3]Department of Psychiatry, Psychotherapy and Psychosomatics, Medical Faculty, RWTH Aachen University, Aachen, Germany

[4]Department of Physics, Faculty 1, RWTH Aachen University, Aachen, Germany

*Correspondence to: Maximilian Schmidt
Forschungszentrum Jülich
52425 Jülich, Germany
max.schmidt@fz-juelich.de

Abstract

Understanding the relationship between structure and dynamics of the mammalian cortex is a key challenge of neuroscience. So far, it has been tackled in two ways: by modeling neurons or small circuits in great detail, and through large-scale models representing each area with a small number of differential equations. To bridge the gap between these two approaches, we construct a spiking network model extending earlier work on the cortical microcircuit by Potjans & Diesmann (2014) to all 32 areas of the macaque visual cortex in the parcellation of Felleman & Van Essen (1991). The model takes into account specific neuronal densities and laminar thicknesses of the individual areas. The connectivity of the model combines recently updated binary tracing data from the CoCoMac database (Stephan et al., 2001) with quantitative tracing data providing connection densities (Markov et al., 2014a) and laminar connection patterns (Stephan et al., 2001; Markov et al., 2014b). We estimate missing data using structural regularities such as the exponential decay of connection densities with distance between areas (Ercsey-Ravasz et al., 2013) and a fit of laminar patterns versus logarithmic ratios of neuron densities. The model integrates a large body of knowledge on the structure of macaque visual cortex into a consistent framework that allows for progressive refinement.

Introduction

In the study of cortical dynamics by bottom-up neuronal network simulations, two basic approaches have been employed. In the first approach, each neuron is modeled explicitly. There is a wealth of such models ranging from the level of local microcircuits to small numbers of interconnected areas, with varying degrees of detail both on the single-cell level and in the connectivity. These models have for instance addressed the statistical properties of neuronal spiking (Traub et al., 2005; Haeusler et al., 2009), slow oscillations arising in thalamo-cortical circuits (Hill & Tononi, 2005), responses to external stimuli (Rasch et al., 2011), and the influence of local connectivity structure on dynamics (Haeusler et al., 2009; Voges & Perrinet, 2012).

Another type of models simulates the large-scale dynamics of the cortex by representing single areas or populations with highly simplified models that reduce the ensemble dynamics to few differential equations, such as Wilson-Cowan (Deco et al., 2009) or Kuramoto oscillators (Cabral et al., 2011). We also include in this category models where entire areas are represented by small numbers of spiking neurons (Deco & Jirsa, 2012). These models are able to reproduce several aspects of large-scale brain activity, including resting-state oscillations between subnetworks at $\sim$0.1 Hz (Fox et al., 2005; Fox & Raichle, 2007).

Considering current theories and experimental findings about cortical function, both types of models have their limitations. Cortical processing is not restricted to one or few areas; it is rather the result of complex interactions between many areas involving feed-forward and feedback processes (Lamme et al., 1998; Pascual-Leone & Walsh, 2001; Riesenhuber & Poggio, 1999; Rao & Ballard, 1999; Bastos et al., 2015). On the other hand, the high degree of connectivity within areas (Angelucci et al., 2002; Markov et al., 2011) hints at an important role for local processing. Therefore, a better understanding of brain function and dynamics can be expected from multi-scale models that combine the detailed features of local microcircuits with realistic interactions between areas. Another advantage of multi-scale modeling is that it enables the equivalence between simplified population models and models at cellular resolution to be tested, instead of assuming it a priori.

The simulation of large-scale neuronal networks at cellular resolution has been hindered by two major obstacles which are now gradually being overcome. First, simulating these models requires large computational resources on high-performance clusters or even supercomputers, and the simulation technology has to be optimized in order to use these resources in an efficient way. Recently, important progress in simulation technology (Kunkel et al., 2014) has been achieved and demonstrated for the NEST simulator (Gewaltig & Diesmann, 2007). The capability to simulate networks comprising up to $1.7 \cdot 10^9$ neurons and 10^{13} synapses has been shown using the K supercomputer in Kobe, Japan (RIKEN BSI, 2013). Second, gaps in the anatomical knowledge have prevented the consistent definition of multi-area models. The development of the CoCoMac database (Stephan et al., 2001; Bakker et al., 2012) has facilitated the systematic gathering of connectivity data for the macaque cortex, and recent studies have delivered quantitative data about cortico-cortical connections in the macaque brain including laminar information (Markov et al., 2014a,b). Furthermore, an extensive brain simulation initiative within the European Human Brain Project (HBP) sets out to deliver a comprehensive infrastructure which hosts data, data-fusion algorithms and simulation engines at scales ranging from gene networks and synapse distributions to gross anatomical features (Kandel et al., 2013; Tiesinga et al., 2015). However, data concerning cortical architecture remain incomplete, so that it remains necessary to predict missing data using regularities to fully specify large-scale cortical network models.

As a consequence of these difficulties, few simulation studies of large-scale spiking networks have been

conducted to date. A large-scale network based on macaque data has recently been successfully simulated using the Compass simulator (Preissl et al., 2012). The network comprised $\sim 65 \cdot 10^9$ neurons and $\sim 16 \cdot 10^{12}$ synapses, corresponding to an average indegree of ~ 250, which is far less than the actual $\sim 10^4$ synapses a neuron in the macaque cortex typically receives. The simulations were carried out on a neuromorphic hardware restricting synaptic weights to a fixed value for all outgoing connections of a neuron. Moreover, the authors used binary connectivity data from CoCoMac while in fact connection densities vary by several orders of magnitude (Markov et al., 2014a). Another large-scale cortical network model was developed by Izhikevich & Edelman (2008) who studied spiking patterns, oscillations and propagating waves in a network model comprising 1 million multi-compartmental spiking neurons connected via $\sim 0.5 \times 10^9$ synapses. For computational reasons, the synaptic density was heavily reduced, so that each neuron received on average only 500 synapses. Such downscaling generally affects network dynamics already in terms of second-order statistics, leading to quantitatively and sometimes even qualitatively incorrect results (van Albada et al., 2015).

In the present model, we more closely approximate the numbers of synapses per neuron found in the primate brain. The model builds on a recently published model simulating a canonical microcircuit of a $1\,\mathrm{mm}^2$ cortical patch containing about 10^5 neurons (Potjans & Diesmann, 2014), which extends the classical balanced random network model (Brunel, 2000) to multiple populations (see also Potjans & Diesmann, 2013). This is the smallest network size where realistic connection probabilities ($\sim 10\%$) and realistic numbers of inputs per neuron ($\sim 10,000$) can be combined. Its main feature is the population-specific connectivity map, synthesized from a combination of electrophysiological recordings and reconstructions of axonal and dendritic trees. The model reproduces patterns of spontaneous spiking activity across populations, and provides insight into the laminar processing of transient thalamocortical input. However, in the $1\,\mathrm{mm}^2$ patch, only $\sim 50\%$ of the incoming synapses of each neuron are actually simulated in the model, while the rest originates outside of the microcircuit and is therefore replaced by stochastic input. Increasing the size of the simulated patch leads to the integration of more intra-areal synapses into the model, while including more cortical areas adds cortico-cortical synapses. In both cases, the influence of random input is reduced, and the resulting models more accurately reflect recurrent interactions.

We here focus on the extension to multiple areas, yielding a model encompassing the entire vision-related cortex parcellated into 32 areas after Felleman & Van Essen (1991). We concentrate on the macaque monkey both because of the availability of extensive connectivity information, and because of the relative similarity of macaque and human brains (Goulas et al., 2014; Li et al., 2013). Like the microcircuit model of Potjans & Diesmann (2014), the multi-area model combines simple single-neuron dynamics with complex structural connectivity and thereby allows us to study the influence of the connectivity itself on the network dynamics. Neurons are represented by the leaky integrate-and-fire model with identical intrinsic properties connected via current-based static synapses. The connectivity map is adapted from the microcircuit model complemented with anatomical data about neuron densities and inter-areal connections (Stephan et al., 2001; Markov et al., 2014a). A new release of CoCoMac is used (Bakker et al., 2012), in which mappings between parcellation schemes are revisited to ensure a consistent transfer of connections to the FV91 atlas. The use of tracing data avoids the unreliability especially for long-range connections of diffusion MRI (Thomas et al., 2014), on which the connectivity in most multi-area modeling work is based.

Our model bridges the gap between single-area or -population models on the one hand and macroscopic brain models on the other, and enables us to relate mechanisms on multiple scales, such as the propagation of transient input inside areas (Schroeder et al., 1998; Sakata & Harris, 2009) and interactions between areas (Shen et al., 2012, 2015). We here present the model construction, leaving an account of its dynamical properties to future work. Preliminary results have been presented in abstract form (Schmidt et al., 2013, 2014).

Construction of the model

A: Model summary	
Populations	254 populations: 32 areas with eight populations each (area TH: six)
Topology	—
Connectivity	area- and population-specific but otherwise random
Neuron model	leaky integrate-and-fire (LIF), fixed absolute refractory period (voltage clamp)
Synapse model	exponential postsynaptic currents
Plasticity	—
Input	independent homogeneous Poisson spike trains
Measurements	spiking activity, membrane potentials

B: Populations			
Type	**Elements**	**Number of populations**	**Population size**
Cortex	LIF neurons	32 areas with eight populations each (area TH: six), two per layer	N (area- and population-specific)

C: Connectivity	
Type	source and target neurons drawn randomly with replacement (allowing autapses and multapses) with area- and population-specific connection probabilities
Weights	fixed, drawn from normal distribution with mean w and standard deviation $\delta w = 0.1w$; 4E to 2/3E increased by factor 2 (cf. Potjans & Diesmann, 2014); weights of inhibitory connections increased by factor g; excitatory weights < 0 and inhibitory weights > 0 are redrawn
Delays	fixed, drawn from Gaussian distribution with mean d and standard deviation $\delta d = 0.5d$; delays of inhibitory connections factor 2 smaller; delays rounded to the nearest multiple of the simulation step size $h = 0.1\,\mathrm{ms}$, inter-areal delays derived from distances with constant transmission speed; delays $< 0.1\,\mathrm{ms}$ before rounding are redrawn

D: Neuron and synapse model	
Name	LIF neuron
Type	leaky integrate-and-fire, exponential synaptic current inputs
Subthreshold dynamics	$\frac{\mathrm{d}V}{\mathrm{d}t} = -\frac{V-E_\mathrm{L}}{\tau_\mathrm{m}} + \frac{I_\mathrm{s}(t)}{C_\mathrm{m}}$ if $(\mathrm{t} > \mathrm{t}^* + \tau_\mathrm{r})$ $V(t) = V_\mathrm{r}$ else $I_\mathrm{s}(t) = \sum_{i,k} w_k\, e^{-(t-t_i^k)/\tau_\mathrm{s}} \Theta(t - t_i^k)$ k: neuron index, i: spike index
Spiking	If $V(t-) < \theta \wedge V(t+) \geq \theta$ 1. set $t^* = t$, 2. emit spike with time stamp t^*

E: Input		
Type	**Target**	**Description**
Background	LIF neurons	independent Poisson spikes (see Table S1)

F: Measurements
Spiking activity and membrane potentials from a subset of neurons in each population

Table 1: Model description after Nordlie et al. (2009).

The model comprises 32 areas of the macaque cortex involved in visual processing in the parcellation of Felleman & Van Essen (1991), in the following referred to as FV91. Each area consists of 8 populations representing layers 2/3, 4, 5 and 6 each with an excitatory and an inhibitory population, with the exception of area TH which does not contain a granular layer. The model for each area is based on that of Potjans & Diesmann (2014), which we refer to as *the microcircuit model*. Table 1 summarizes the resulting multi-area model, in which each area is represented by a $1\,\mathrm{mm}^2$ patch of cortical surface.

The single-neuron dynamics and the distributions of intra-areal delays correspond to those of Potjans & Diesmann (2014). The neuron and synapse parameters are listed in Table S1. We assume a constant transmission speed of $v_\mathrm{t} = 3.5\,\mathrm{m/s}$ between areas as measured in monkey visual cortex (Girard et al., 2001), and draw the inter-areal delays from a Gaussian distribution with mean $d = s/v_\mathrm{t}$ where s is the distance, and standard deviation $\delta d = d/2$. The distance between each pair of areas is computed as the median of the distances between all vertex pairs of these two areas in their surface representation in F99 space, a standard macaque cortical surface included with Caret (Van Essen et al., 2001), where the vertex-to-vertex distance is the length of the shortest possible path without crossing the cortical surface (Bojak et al., 2011).

In the following, we describe the data integration process leading to population sizes and connection probabilities from a combination of experimental data and statistical regularities.

Neuron numbers

First, we estimate the number of neurons $N(A, i)$ in population i of area A in three steps:

1. Neuronal volume densities provided in a different parcellation scheme (total neuron densities from Hilgetag et al. (2015), laminar-specific data from H. Barbas and C. Hilgetag, personal communication) were mapped to the FV91 scheme and partly estimated using the notion of architectural types. The translation uses the data of the most representative area in the original scheme. The classification of areas into architectural types (Hilgetag et al., 2015) extends a classification previously developed for prefrontal cortex (Barbas, 1986; Barbas & Rempel-Clower, 1997; Dombrowski et al., 2001) to the visual areas. Table 4 of Hilgetag et al. (2015) shows the classification which we translate to our area scheme as detailed in Table S2. The architectural type reflects the distinctiveness of the lamination as well as the degree of development of granular layer 4, with the lowest values corresponding to agranular and dysgranular cortices, and the highest value corresponding to V1. Areas MIP and MDP were not classified due to insufficient data and were manually assigned type 5 like their neighboring area PO, which is similarly involved in visual reaching (Johnson et al., 1996; Galletti et al., 2003), and was placed at the same hierarchical level by Felleman & Van Essen (1991). To estimate neuron densities for areas not included in the data set, we compute the average density of layer v across areas with architectural type α.

2. Total cortical thicknesses $D(A)$ were provided for 14 areas by H. Barbas and C. Hilgetag (personal communication). The data partially overlap with Hilgetag et al. (2015). These show a significant decrease with architectural type. A similar trend was recently demonstrated in MR measurements of cortical thickness (Wagstyl et al., 2015). The total thicknesses of the other 18 areas were estimated using this linear fit. Laminar thicknesses were determined from quantitative data combined with estimates from a large number of micrographs from the literature (Fig. 1). For those areas for which we found no data in the literature, we estimate laminar thicknesses using a linear least-squares fit of per-area average relative thicknesses against architectural type for each layer. Since the thicknesses of L2/3 and L6 relative to the total thickness of cortex show no notable change with architectural type, we filled in missing values using the mean of the known data for these quantities. Relative L4 thickness increases (as expected, since L4 thickness enters into the definition of architectural types) and relative L5 thickness decreases with architectural type. For areas with missing data these linear regression fits are used to compute relative L4 and L5 thicknesses. Absolute thicknesses follow from the product of relative thickness and total thickness. We also tested for a linear trend of total and laminar thicknesses with logarithmized total cell densities, as another correlate of the structural differentiation of areas. This slightly increases the significance of the linear fit for total thicknesses ($r = -0.71$, $p = 0.004$). Similarly, the fit of L4 thicknesses shows higher correlation ($r = 0.87$, $p = 10^{-4}$). However, L5 thicknesses do not reveal a significant trend ($r = -0.32$, $p = 0.32$). Here, we use the linear relationships with architectural types, keeping in mind that the L5 trend merits further investigation.

3. The fraction $\gamma(v)$ of excitatory neurons in layer v is assumed to be identical across areas. For the laminar dependency, the values that Binzegger et al. (2004) observe in cat V1 are used (see Table 2).

layer	$\frac{N_\mathrm{E}}{N_\mathrm{E}+N_\mathrm{I}}$	$\frac{N_\mathrm{I}}{N_\mathrm{E}+N_\mathrm{I}}$
2/3	0.78	0.22
4	0.80	0.20
5	0.82	0.18
6	0.83	0.17

Table 2: Proportions of inhibitory and excitatory neurons in each layer of cat primary visual cortex according to Binzegger et al. (2004).

These data and assumptions deliver the number of neurons in population i of area A,

$$N(A,i) = \rho\left(A, v_i\right) S(A) D\left(A, v_i\right) \cdot \begin{cases} \gamma\left(v_i\right) & \text{if } i \in \mathcal{E} \\ 1-\gamma\left(v_i\right) & \text{if } i \in \mathcal{I} \end{cases}, \tag{1}$$

where v_i denotes the layer of population i, $S(A)$ the surface area of area A computed with the Caret software (Van Essen et al., 2001) on the basis of its representation on the F99 cortical surface (Van Essen, 2002), $D(A, v_i)$ the thickness of layer v_i, and $\mathcal{E}, \mathcal{I}$ the pool of excitatory and inhibitory populations, respectively. Table S3 lists the surface areas $S(A)$ we use in the derivation of the connectivity.

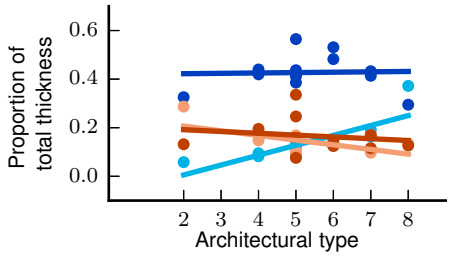

Figure 1: Relative laminar thicknesses vs architectural types. Thickness data compiled from Angelucci et al. (2002); Boussaoud et al. (1990); Eggan & Lewis (2007); Felleman et al. (1997); Lavenex et al. (2002); Markov et al. (2014a); O'Kusky & Colonnier (1982); Petrides & Pandya (1999); Preuss & Goldman-Rakic (1991); Rakic et al. (1991); Rockland (1992); Rozzi et al. (2006). Solid lines are linear least-squares fits (L2/3 (dark blue): $r = 0.03$, $p = 0.92$, L4 (light blue): $r = 0.80$, $p = 0.001$; L5 (orange): $r = -0.55$, $p = 0.08$, L6 (red): $r = -0.17$, $p = 0.62$).

Each neuron in the network receives synapses of four different origins, as sketched in Fig. 2A. In the following, we describe how the counts for each of these synapse types are computed.

Local connectivity

In line with a number of anatomical observations (Harrison et al., 2002; O'Kusky & Colonnier, 1982; Schüz & Palm, 1989; Cragg, 1967), we assume that the total synaptic volume density is constant across areas. Cragg (1967) provides an average indegree in monkey visual cortex of $\sim 5,600$ synapses per neuron while O'Kusky & Colonnier (1982) report $2,300$ synapses per neuron. We take the average $3,950$ of both values as representative for V1. The resulting volume density is $\rho_{\text{syn}} = \frac{3950\, N(V1)}{D(V1)\, S(V1)} = 5.9 \cdot 10^8 \frac{\text{synapses}}{\text{mm}^3}$, which approximately agrees with $6.3 \cdot 10^8 \frac{\text{synapses}}{\text{mm}^3}$ reported for somatosensory cortex of rat by Markram et al. (2015).

The connection probabilities of the microcircuit model listed in Table 5 of Potjans & Diesmann (2014), which have been computed from various anatomical and electrophysiological studies (with large contributions from Binzegger et al., 2004; Thomson & Lamy, 2007), serve as the basis of our calculations. The connectivity between any pair of populations in the model is spatially uniform. However, to derive the corresponding connection probabilities, we approximate the underlying probability C for a given pair of neurons to establish at least one contact as falling off with distance according to a Gaussian probability distribution with standard deviation $\sigma = 297\,\mu$m (Potjans & Diesmann, 2014). To determine average connection probabilities, we approximate each brain area A as a flat disk with (area-specific) radius R and assign polar coordinates r and θ to each neuron. The radius R hence determines the cut-off of the Gaussian distribution and the precise values of the population connectivities. The average connection probability between a pre- and postsynaptic neuron pair is then obtained by integrating over all possible positions of the two neurons:

$$\bar{C}(R) = \frac{C_0}{\pi^2 R^4} \int_0^R \int_0^{2\pi} \int_0^R \int_0^{2\pi} \exp\left[\frac{-\left(r_1^2 + r_2^2 - 2 r_1 r_2 \cos(\theta_1 - \theta_2)\right)}{2\sigma^2}\right] r_1 r_2 \mathrm{d}\theta_1 \mathrm{d}r_1 \mathrm{d}\theta_2 \mathrm{d}r_2\,, \tag{2}$$

where C_0 is the connection probability at zero distance. This can be reduced to a simpler form (Sheng, 1985), reading

$$\bar{C}(R) = \frac{2C_0}{\pi R^2} \int_0^{2R} e^{-r^2/2\sigma^2} \left[4 \arctan\left(\frac{2R - r}{2R + r}\right)^{1/2} - \sin\left(4 \arctan\left[\frac{2R - r}{2R + r}\right]^{1/2}\right)\right] r \mathrm{d}r\,. \tag{3}$$

Averaged across pairs of populations, the value of C_0 is 0.143 (computed from Eq. 8 and Table S1 in Potjans & Diesmann, 2014)). Note that Potjans & Diesmann (2014) use a simpler approach where only the position of one neuron is varied while keeping the other neuron fixed in the center of the disk (Eq. 9 in that paper). Connection probabilities computed with the latter approach are denoted with the subscript

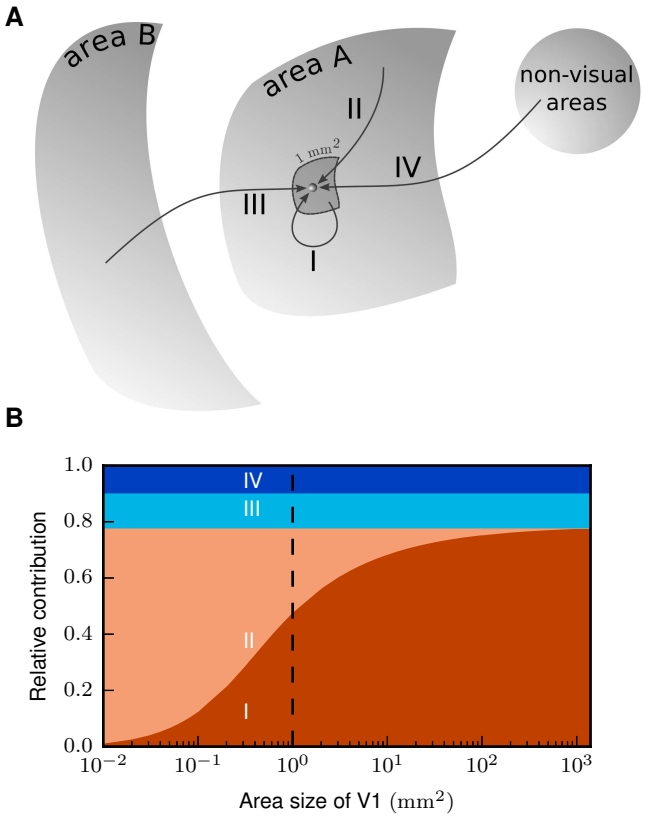

Figure 2: Contributions of different synaptic sources. **A** Scheme of the different types of connections to a cortical neuron. I: Simulated intra-areal synapses, II: Intra-areal synapses from outside the $1\ \mathrm{mm}^2$ patch modeled as Poisson sources, III: Simulated cortico-cortical synapses, IV: Synapses from subcortical and non-visual cortical areas modeled as Poisson sources. **B** Relative contributions to indegrees in V1 (stacked vertically) for increasing cortical surface area (horizontal) covered by the model. The number of simulated intra-areal synapses (red, I) increases at the cost of random input from non-simulated intra-areal synapses (light red, II) while the number of cortico-cortical synapses (light blue, III) and random inputs from subcortical and non-visual cortical areas (blue, IV) stays constant. The vertical dashed line signals the surface area of $1\ \mathrm{mm}^2$ used in the present study.

PD14. Moreover, in the following, we use primes for all variables referring to a network with the laminar distribution of neurons of the microcircuit model.

We use (3) to determine the population-specific spatially averaged connection probabilities. The parameters of the microcircuit model are reported for a $1\ \mathrm{mm}^2$ patch of cortex, corresponding to $R = \sqrt{1/\pi}\,\mathrm{mm}$, which we call R_0. For each source population j and target population i, we first translate the connection probabilities of the $1\ \mathrm{mm}^2$ model to area-dependent R via

$$C'_{ij}(R) = C'_{ij,\mathrm{PD14}}\left(R_0\right) \frac{\bar{C}'(R)}{\bar{C}'_{\mathrm{PD14}}\left(R_0\right)},$$

with $\bar{C}'_{\mathrm{PD14}}(R_0) = 0.066$. From the connection probability, we compute the number of synapses for a projection from population j to i as

$$N_{\mathrm{syn},ij} = \frac{\log\left(1 - C_{ij}\right)}{\log\left(1 - \frac{1}{N_i N_j}\right)},$$

which follows from randomly drawing source and target neurons with replacement (cf. Eq. 1 in Potjans & Diesmann, 2014). The indegree K_{ij} is the number of incoming synapses per target neuron, $N_{\mathrm{syn},ij}/N_i$. In the following, all numbers of synapses $N_{\mathrm{syn}}(A)$ and indegrees $K_{ij}(A)$ are area-specific. For simplicity, we leave out the argument A. Since mean synaptic inputs are proportional to the indegrees, we consider them as a defining characteristic of the local circuit and preserve their relative values to approximately preserve relative influences between populations when adjusting the model to area-specific neuron densities,

$$\frac{K_{ij}(R)}{K_{kl}(R)} = \frac{K'_{ij}(R)}{K'_{kl}(R)} \;\; \forall i,j,k,l$$
$$\Leftrightarrow K_{ij}(R) = c_A(R) K'_{ij}(R) \;\; \forall i,j\,, \tag{4}$$

where $c_A(R)$ is an area-specific conversion factor, which is larger for areas with smaller neuron densities because of the assumption of a constant synaptic volume density. The total number of synapses local to the patch (type I) is the sum over the projections between all populations of the area:

$$N_{\mathrm{syn,I}}(R) = \sum_{i,j} N_i(R) K_{ij}(R) = c_A(R) \sum_{i,j} N_i(R) K'_{ij}(R)\,.$$

We thus obtain $c_A(R)$ by determining $N_{\mathrm{syn,I}}$. To this end, we use retrograde tracing data from Markov et al. (2011) consisting of fractions of labeled neurons (FLN) per area as a result of injections into one area at a time. The fraction intrinsic to the injected area, FLN_{i}, is approximately equal for all 9 areas where this fraction was determined, with a mean of 0.79. We translate this into numbers of synapses by assuming that, on average, each labeled neuron establishes the same number of synapses in the injected area, so that the proportion of synapses of type I is 0.79 for the full area size. For areas modeled with reduced size, this fraction is smaller because, in that case, synapses of both type I and II contribute to the value of 0.79 (Fig. 2B). We approximate the increasing contribution of type I synapses with the modeled area size as the increase in indegrees averaged over population pairs,

$$\frac{N_{\mathrm{syn,I}}(R)/N_{\mathrm{syn,tot}}(R)}{N_{\mathrm{syn,I}}(R_{\mathrm{full}})/N_{\mathrm{syn,tot}}(R_{\mathrm{full}})} \;\; = \;\; \left\langle \frac{K_{ij}(R)}{K_{ij}(R_{\mathrm{full}})} \right\rangle_{ij} = \left\langle \frac{K'_{ij}(R)}{K'_{ij}(R_{\mathrm{full}})} \right\rangle_{ij},$$

where in the last step we use (4). Using $N_{\mathrm{syn,I}}(R_{\mathrm{full}})/N_{\mathrm{syn,tot}}(R_{\mathrm{full}}) = FLN_{\mathrm{i}}$, we obtain

$$N_{\mathrm{syn,I}}(R) = N_{\mathrm{syn,tot}}(R)\, FLN_{\mathrm{i}} \left\langle \frac{K'_{ij}(R)}{K'_{ij}(R_{\mathrm{full}})} \right\rangle_{ij},$$

where $N_{\mathrm{syn,tot}}(R) = \rho_{\mathrm{syn}} \pi R^2 D$ with D the total thickness of the given area. The conversion factor can thus be obtained with

$$c_A(R) = \frac{N_{\mathrm{syn,tot}}(R)}{\sum_{i,j} N_i(R) K'_{ij}(R)}\, FLN_{\mathrm{i}} \left\langle \frac{K'_{ij}(R)}{K'_{ij}(R_{\mathrm{full}})} \right\rangle_{ij}.$$

We substitute this into (4) for the modeled areas where $R = R_0$ and obtain the population-specific indegrees for synapses of type I:

$$K_{ij,\mathrm{I}} := K_{ij}\,(R = R_0) \tag{5}$$

Cortico-cortical connectivity

In the model, all synapses onto a neuron in the target area originate exclusively in the 1 mm^2 patch representing the source area. This is similar to assuming that the connections between areas are parallel on the 1 mm^2 scale. In nature, these connections exhibit a certain degree of spatial convergence and divergence (Colby et al., 1988; Salin et al., 1989; Gattass et al., 1997; Markov et al., 2014b). However, our choice enhances the interactions between areas and counteracts the dilution of inter-areal influences due to the lack of spatial organization within the modeled patch.

As a starting point, we determine whether a pair of areas is connected using the union of all connections available in the FV91 scheme in the CoCoMac database (Stephan et al., 2001; Bakker et al., 2012; Suzuki & Amaral, 1994a; Felleman & Van Essen, 1991; Rockland & Pandya, 1979; Barnes & Pandya, 1992) (Fig. 3A, see supplementary section "Processing of CoCoMac data" for details) and all connections reported by Markov et al. (2014a). We use a new release of CoCoMac, in which mappings from brain regions in other nomenclatures were scrutinized to ensure a consistent transfer of connections into the FV91 name space. We then determine the population-specific numbers of modeled cortico-cortical synapses in three steps: 1. determining the area-level connectivity; 2. distributing synapses across layers; 3. assigning synapses to target neurons.

For the first step, we compute the total numbers of synapses formed between each pair of areas using retrograde tracing data from Markov et al. (2014a). The data consist of fractions of labeled neurons $FLN_{AB} = NLN_{AB}/\sum_{B'} NLN_{AB'}$, with NLN the number of labeled neurons in area B following an injection in area A. Markov et al. (2014a) used a parcellation scheme called M132 which is also available as a cortical surface, both in native and in F99 space. On the target side we use the coordinates of the

injection sites registered to the F99 atlas available via the Scalable Brain Atlas (Bakker et al., 2015) to identify the equivalent area in the FV91 parcellation (cf. Table S4). There is data for 11 visual areas in the FV91 scheme with repeat injections in six areas, for which we take the arithmetic mean. To map data on the source side from the M132 atlas to the FV91 parcellation, we count the number of overlapping triangles on the F99 surface between any given pair of regions and distribute the FLN proportionally to the amount of overlap, using tools available at the CoCoMac site (`http://cocomac.g-node.org/services/f99_region_overlap.php`). Fig. 3B shows the result of this mapping procedure. To estimate values for the areas not included in the data set, we make use of a roughly exponential fall-off of connectivities with distance (Ercsey-Ravasz et al., 2013), modeled as

$$FLN_{AB} = C \cdot \exp\left(-\lambda d_{AB}\right) \ . \tag{6}$$

A linear least-squares fit of the logarithm of the FLN (Fig. 3C) predicts missing values. The total number of synapses $N_{\mathrm{syn},AB}$ between each pair of areas $\{A, B\}$ is assumed to be proportional to the number of labeled neurons NLN_{AB} and thus to FLN_{AB},

$$\frac{N_{\mathrm{syn},AB}}{\underbrace{\sum_{B'} N_{\mathrm{syn},AB'}}_{=N_{\mathrm{syn,tot},A}}} = \frac{NLN_{AB}}{\sum_{B'} NLN_{AB'}} = \frac{FLN_{AB}}{\sum_{B'} FLN_{AB'}}. \tag{7}$$

This corresponds to individual neurons in each source area (including area A itself) on average establishing the same number of synapses in the target area A. For each target area, the FLN in the model should add up to the total fraction of connections coming from visual cortical areas. However, this fraction is not known a priori. To provide a normalization, we therefore consider also non-visual areas, for which distances are available and for which we can hence also estimate the FLN. The total fraction of all connections from subcortical regions was found to average 1.3 % in eight cortical areas (Markov et al., 2011). This allows us to normalize the combined FLN from all cortical areas as $\sum_B FLN_{AB} = 1 - FLN_{\mathrm{i}} - 0.013$, where B here runs over both modeled and non-modeled cortical areas. Fig. 3D shows the result of combining the binary information from CoCoMac with measured and estimated FLN to a connectivity matrix on the area level.

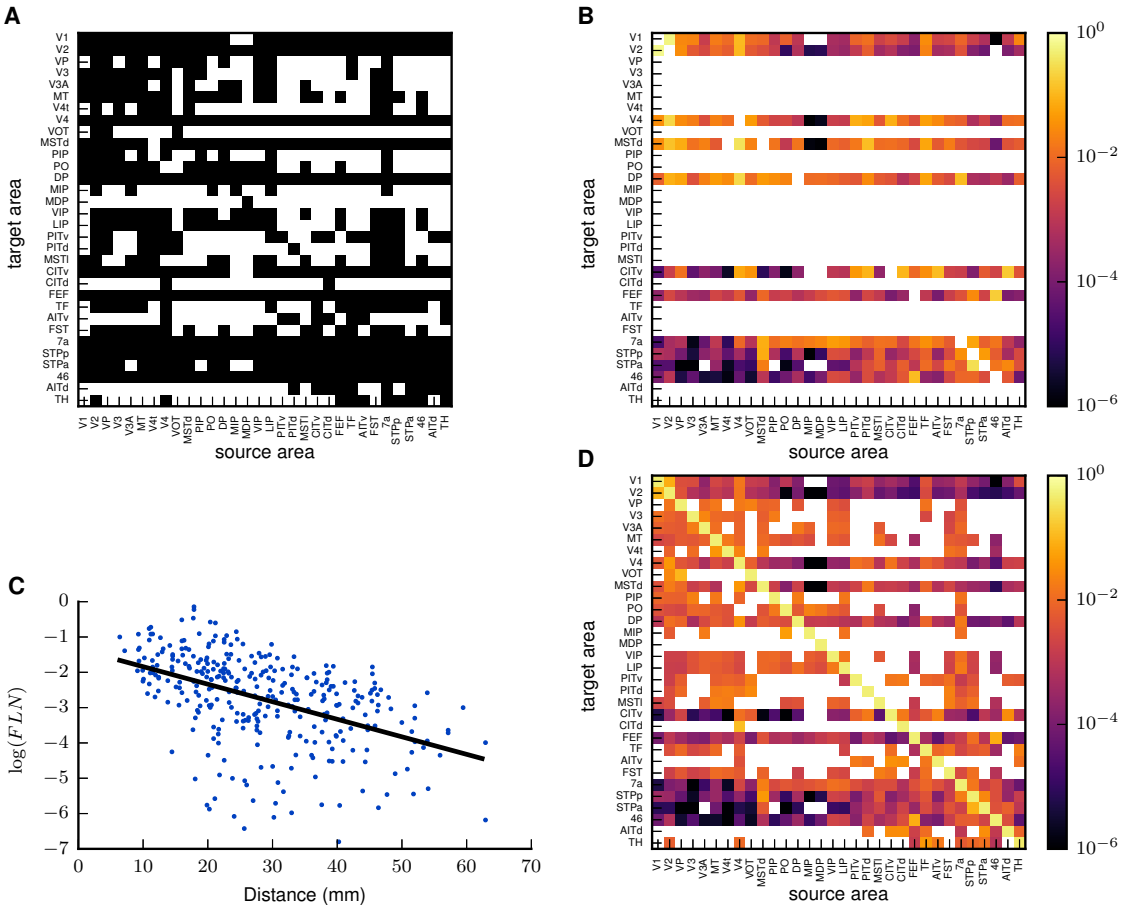

Figure 3: Construction of the connectivity map at area level. **A** Binary connectivity information from the CoCoMac database. Black, existing connections; white, absent connections. **B** Fractions of labeled neurons (FLN) from Markov et al. (2014a) mapped to the parcellation scheme of Felleman & Van Essen (1991). **C** Connection densities fall off approximately exponentially with inter-area distance. Distances computed as median vertex distance in the cortical surface representation of the M132 areas. Black line: linear regression with $\log(FLN) = \log(C) - \lambda d$ ($C = 0.045, \lambda = 0.11, p = 10^{-19}$; cf. (6)). **D** Area-level connectivity of the model, based on data shown in panels A-C, expressed as relative indegrees for each target area.

As a next step, we determine the distribution of connections across source and target layers. Cortico-cortical connections tend to follow specific laminar patterns that are related to the differences in architectural types or neuron densities of the areas (Hilgetag et al., 2015), and consequently also to their relative positions in an approximate processing hierarchy (Felleman & Van Essen, 1991). On the source side, the laminar pattern of projections can be expressed as the fraction of supragranular labeled neurons (SLN) in retrograde tracing experiments (Markov et al., 2014b). To determine the SLN entering into the model, we follow a similar procedure as for the FLN: We use the exact coordinates of the injections to determine the corresponding target area A in the FV91 parcellation, and in case of repeat injections into the given target area, for each pair of areas we take the mean SLN across injections. To map the data from the M132 parcellation to the FV91 scheme, we weight the SLN by the overlap $c_{B,\beta}$ between area β in the former and area B in the latter scheme and the FLN to take into account the overall strength of the connection, so that

$$SLN_{AB} = \frac{\sum_\beta c_{B,\beta} FLN_{A,\beta} SLN_{A,\beta}}{\sum_\beta c_{B,\beta} FLN_{A,\beta}} .$$

Since SLN data are not available for all pairs of areas, we estimate missing values using a sigmoidal relation between SLN and the logarithmized ratio of overall cell densities of the two areas (Fig. 4A). This

is similar to the relation between SLN and hierarchical distances found by Markov et al. (2014b), but avoids the cyclicity of estimating SLN from the hierarchy which itself was obtained using the SLN data. A relationship between laminar patterns and log ratios of neuron densities was suggested by Beul et al. (2015). Following Markov et al. (2014b), we use a beta-binomial generalized linear model (GLM), which assumes the numbers of labeled neurons in the source areas to sample from a beta-binomial distribution (e.g. Weisstein, 2005). This distribution arises as a combination of a binomial distribution with parameter p giving the probability of supragranular labeling within each source area, and a beta distribution of p across areas with dispersion parameter ϕ. With the probit link function g (e.g. McCulloch et al., 2008), the relation between the measured SLN and the log ratio ℓ of neuron densities for each pair of areas becomes

$$g(SLN) = a_0 \begin{pmatrix} 1 \\ \vdots \\ 1 \end{pmatrix} + a_1 \ell, \tag{8}$$

where ℓ and SLN are vectors and $\{a_0, a_1\}$ are scalar fit parameters. To fit SLN to logarithmized ratios of cell densities, we map the FV91 areas to the Markov et al. (2014b) scheme with the overlap tool of CoCoMac (see above) and compute the cell density of each area in the M132 scheme as a weighted average over the relevant FV91 areas (each with cell density either measured, or estimated according to its architectural type). For areas with identical names in both schemes, we simply take the neuron density as determined in the FV91 scheme. Fig. 4A shows the result of the SLN fit carried out in R (R Core Team, 2015) with the betabin function of the aod package (Lesnoff & Lancelot, 2012). In contrast to Markov et al. (2014b), who excluded certain areas when fitting SLN vs. hierarchical distances in view of ambiguous hierarchical relations, we take all data points into account to obtain a simple and uniform rule.

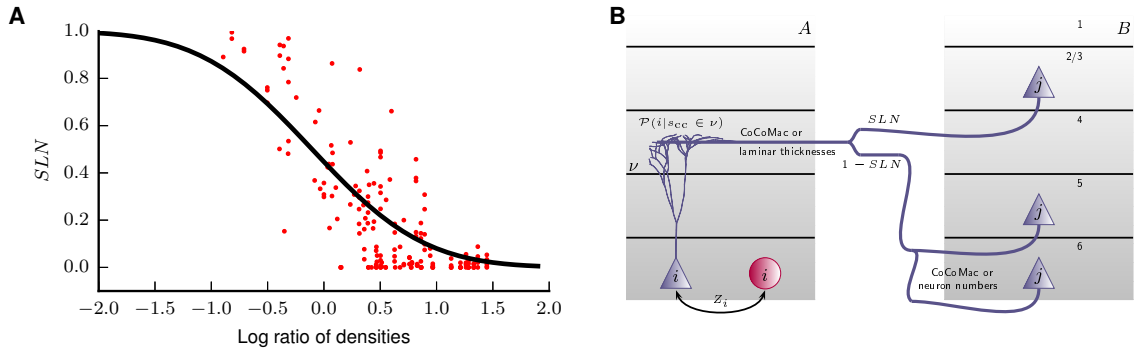

Figure 4: Laminar patterns of cortico-cortical connections. A Fractions of source neurons in supragranular layers depend sigmoidally on the logarithmized ratio of the overall cell densities of the two areas. SLN data from Markov et al. (2014b), neuron densities from Hilgetag et al. (2015). Black curve: fit using a beta-binomial generalized linear model (8) ($a_0 = -0.134$, $a_1 = -1.27$, $\phi = 0.212$). **B** Schematic illustration of the procedure for distributing synapses across layers. Source neuron j from area B sends an axon to layer v of area A where a cortico-cortical synapse s_{CC} is formed at the dendrite of neuron i. The inclusion of a layer in a source or target pattern is determined by CoCoMac data if available, and otherwise based on measured or estimated SLN. The diagram illustrates the distribution of synapses for connected sets of layers. To distribute synapses across excitatory populations in the sending area, SLN is combined with projection densities from CoCoMac if available, or with neuron numbers as proportionality factors. Layer 1 is only modeled as a target layer where synapses are formed and associated with cell bodies in layers $2-6$. In the target area, synapses are distributed across the layers contained in the target pattern using projection densities from CoCoMac if available, or in proportion to laminar thicknesses. The synapses are then attributed to neurons with the help of data from Binzegger et al. (2004). Finally, synapses are re-distributed between excitatory and inhibitory neurons such that $95\,\%$ of synapses target excitatory neurons. See (13) for the formal definitions.

As a further step toward determining laminar distributions of synapses, we combine the measured or estimated SLN with data from CoCoMac. The SLN data and CoCoMac complement each other, with the SLN being quantitatively more precise and CoCoMac containing more detailed laminar patterns.

Specifics of the processing of the laminar CoCoMac data are given in supplementary section "Processing of CoCoMac data". CoCoMac gives the connection strength $\alpha(v)$ of a layer v on a rough quantitative scale, ranging from 0 (absent) to 3 (strong) in integer steps. To distribute synapses between layers, we assume that the connection strengths from CoCoMac represent numbers of synapses in orders of magnitude. The inclusion of a layer in the source pattern P_s is based on CoCoMac (Felleman & Van Essen, 1991; Barnes & Pandya, 1992; Suzuki & Amaral, 1994b; Morel & Bullier, 1990; Perkel et al., 1986; Seltzer & Pandya, 1994) if the corresponding data is available (this is the case for 45 % of all cortico-cortical connections); otherwise, we include layers 2/3, 5 and 6 in the calculation. The exclusion of granular layer 4 from the source pattern is in line with most anatomical observations (Felleman & Van Essen, 1991). Furthermore, we model cortico-cortical connections as emanating from excitatory neurons only, which is a good approximation to experimental findings (Salin & Bullier, 1995; Tomioka & Rockland, 2007). If a layer is included in the source pattern, we assign a fraction of the total outgoing synapses to it according to the SLN. Since the SLN does not further distinguish between the infragranular layers 5 and 6, we use the rough connection densities from CoCoMac for this purpose when available, and otherwise we assume a constant outdegree, distributing synapses in proportion to the numbers of neurons. On the target side, we determine the pattern of target layers P_t from anterograde tracer studies contained in CoCoMac (Jones et al., 1978; Rockland & Pandya, 1979; Morel & Bullier, 1990; Webster et al., 1991; Felleman & Van Essen, 1991; Barnes & Pandya, 1992; Distler et al., 1993; Suzuki & Amaral, 1994b; Webster et al., 1994), which are available for 29 % of all cortico-cortical connections. For connections without laminar information on the target side, we use termination patterns suggested by the SLN based on a relationship between source and target patterns. Using the terminology of visual hierarchies, we denote projections with low, intermediate, and high SLN respectively as feedback, lateral, and feedforward projections. A finer classification may be obtained by simultaneously considering target patterns (Felleman & Van Essen, 1991, Figure 3). We take $SLN < 0.35$ to correspond to feedback projections, $SLN > 0.65$ to feedforward projections and $SLN \in [0.35, 0.65]$ to lateral projections. Feedforward projections terminate preferentially in layer 4 (F), feedback projections tend to have a multilaminar (M) termination pattern, and lateral projections tend to have a columnar (C) termination pattern encompassing all layers (Felleman & Van Essen, 1991). In this case, the termination pattern P_t can thus be of the following types:

$$\begin{aligned} F =& \{4\} \text{ for } SLN > 0.65 \\ M =& \{1, 2/3, 5, 6\} \text{ for } SLN < 0.35 \\ C =& \{1, 2/3, 4, 5, 6\} \text{ for } SLN \in [0.35, 0.65] \end{aligned} \quad , \tag{9}$$

and we distribute synapses among the layers in the termination pattern in proportion to their thickness.

Since we use a point neuron model, we have to account for the possibly different laminar positions of cell bodies and synapses. The data of Binzegger et al. (2004) deliver three quantities that allow us to relate synapse to cell body locations. The first is the probability $\mathcal{P}(s_\mathrm{cc}|c_\mathrm{B} \bigcap s \in v)$ for a synapse in layer v on a cell of type c_B (e.g., a pyramidal cell with soma in layer 5) to be of cortico-cortical origin. Second, Binzegger et al. (2004) provide the relative occurrence $\mathcal{P}(c_\mathrm{B})$ of the cell type c_B, and third, the total numbers of synapses $N_\mathrm{syn}(v, c_\mathrm{B})$ in layer v onto the given cell type. We map these data to our model by computing the conditional probability $\mathcal{P}(i|s_\mathrm{cc} \in v)$ for the target neuron to belong to population i if a cortico-cortical synapse s_cc is located in layer v. This probability equals the sum of probabilities that a synapse is established on the different Binzegger subpopulations making up our populations,

$$\mathcal{P}(i|s_\mathrm{cc} \in v) = \mathcal{P}(\bigcup_{c_\mathrm{B} \in i} c_\mathrm{B}|s_\mathrm{cc} \in v) = \sum_{c_\mathrm{B} \in i} \mathcal{P}(c_\mathrm{B}|s_\mathrm{cc} \in v)\,. \tag{10}$$

where

$$\mathcal{P}(c_\mathrm{B}|s_\mathrm{cc} \in v) = \frac{\mathcal{P}(c_\mathrm{B} \bigcap s_\mathrm{cc} \in v)}{\mathcal{P}(s_\mathrm{cc} \in v)}\,. \tag{11}$$

The numerator gives the joint probability that a cortico-cortical synapse is formed in layer v on cell type c_B,

$$\mathcal{P}(c_\mathrm{B} \bigcap s_\mathrm{cc} \in v) = \frac{N_\mathrm{syn,CC}(v, c_\mathrm{B})\mathcal{P}(c_\mathrm{B})}{\sum_{v', c'_\mathrm{B}} N_\mathrm{syn,CC}(v', c'_\mathrm{B})\mathcal{P}(c'_\mathrm{B})}\,, \tag{12}$$

and the denominator equals the probability of finding a cortico-cortical synapse in layer v, which is computed by summing over cell types,

$$\mathcal{P}(s_\mathrm{cc} \in v) = \sum_{c_\mathrm{B}} \mathcal{P}(c_\mathrm{B} \bigcap s_\mathrm{cc} \in v)\,.$$

$N_{\mathrm{syn,CC}}(v, c_{\mathrm{B}})$ represents the number of cortico-cortical synapses in layer v on cell type c_{B},

$$N_{\mathrm{syn,CC}}(v, c_{\mathrm{B}}) = \mathcal{P}(s_{\mathrm{cc}}|c_{\mathrm{B}} \bigcap s \in v)\, N_{\mathrm{syn}}(v, c_{\mathrm{B}})\, \mathcal{P}(c_{\mathrm{B}})\,,$$

which can be directly determined from the data. Combining these equations, we obtain the number of cortico-cortical (Type III) synapses from excitatory population j of area B to population i of area A (cf. Fig. 4B):

$$N_{\mathrm{syn,III}}(i, A, j, B) = \underbrace{Z_i \sum_{v \in P_{\mathrm{t}}} Y_v\, \mathcal{P}(i|s_{\mathrm{cc}} \in v)}_{\text{target side}} \underbrace{X_j}_{\text{source side}} N_{\mathrm{syn,III}}(A, B)\,, \tag{13}$$

$$\text{with } X_j = \begin{cases} SLN & \text{if } j \in S \bigcap P_{\mathrm{s}} \\ (1-SLN)\frac{10^{\alpha(v_j)}}{\sum_{j' \in I,\, \alpha(v_{j'})>0} 10^{\alpha(v_{j'})}} & \text{if } j \in I \text{ and } \alpha(v_j) > 0 \\ (1-SLN)\frac{N(A,j)}{\sum_{j' \in I} N(A,j')} & \text{if } j \in I \bigcap P_{\mathrm{s}} \text{ but no CoCoMac data available} \\ 0 & \text{if } j \notin P_{\mathrm{s}} \end{cases},$$

$$\text{and } Y_v = \begin{cases} \frac{10^{\alpha(v)}}{\sum_{\alpha(v')>0} 10^{\alpha(v')}} & \text{if } \alpha(v) > 0 \\ \frac{D(A,v)}{\sum_{v'} D(A,v')} & \text{if no CoCoMac data available} \end{cases}.$$

Here, $S = 2/3\mathrm{E}$ and $I = \{5E, 6E\}$ respectively denote the supragranular and infragranular excitatory populations. Z_i is an additional factor which takes into account the experimentally found phenomenon of E-I-specificity in feedback connections. Various studies have found that cortico-cortical feedback connections preferentially target excitatory neurons rather than inhibitory neurons (Johnson & Burkhalter, 1996, 1997; Anderson et al., 2011). Z_i is area-specific and depends on the excitatory or inhibitory nature of the target population, but not on the target layer. Different values for the proportion of excitatory targets have been found, ranging between 87 % and 98 %. As a representative value, we choose a fraction of 93 % of connections targeting excitatory population in the target area. For each feedback connection in the model, we thus redistribute the synapses across the excitatory and inhibitory target populations and determine Z_i such that

$$\frac{\sum_{i \in \mathcal{E}} \sum_j N_{\mathrm{syn,III}}(i, A, j, B)}{N_{\mathrm{syn,III}}(A, B)} = 0.93\,.$$

Fig. S1 shows the resulting connection probabilities between all pairs of populations in the model.

External, random input

Finally, inputs at synapses formed outside the scope of our model, i.e., white-matter synapses from non-cortical or non-visual cortical areas as well as gray-matter synapses formed by cells outside the $1\,\mathrm{mm}^2$ patch, are replaced by Poisson spike trains. The external inputs to each population of the microcircuit model of Potjans & Diesmann (2014) are estimated as a sum over gray- and white-matter inputs and thalamic afferents, and are representative of V1. However, corresponding experimental data are not consistently available across the areas of our model. Furthermore, since laminar patterns of external inputs from cortical areas (Markov et al., 2014b) as well as from subcortical regions such as pulvinar (Felleman & Van Essen, 1991; Rockland et al., 1999) differ between areas, we cannot simply copy the numbers for V1 to the remaining areas. In the absence of area-specific data, we use a simple scheme: For each area, we compute the total number of external synapses as the difference between the total number of synapses and those of type I and III and distribute these such that all neurons in the given area have the same indegree for Poisson sources. The only exception is that in area TH, we compensate for the missing granular layer 4 by increasing the external drive onto populations 2/3E and 5E by 20 %.

Conclusion

In this report, we present the construction of a multi-area model of macaque visual cortex in a modular and algorithmic manner facilitating further refinements as new data become available. The resulting formal network specification enables simulations of the spiking dynamics using the NEST simulator (Gewaltig & Diesmann, 2007). Mean-field theory supports the systematic investigation of the link between structure and dynamics (Schuecker et al., 2015), exploiting the fact that insights from two-population balanced random network models generalize to multi-population networks (Potjans & Diesmann, 2013). Thus, the

present study lays the foundation for further work describing the dynamical behavior of the model and its relation to brain activity measured in experiments.

Funding

This work was supported by the Helmholtz Portfolio Supercomputing and Modeling for the Human Brain (SMHB), European Union (BrainScaleS, grant 269921 and Human Brain Project, grant 604102), the Jülich Aachen Research Alliance (JARA), and computing time granted by the JARA-HPC Vergabegremium and provided on the JARA-HPC Partition part of the supercomputer JUQUEEN (Jülich Supercomputing Centre, 2015) at Forschungszentrum Jülich (VSR computation time grant JINB33).

Acknowledgements

We thank Jannis Schuecker and Moritz Helias for discussions; Claus Hilgetag and Sarah Beul for discussions on cortical architecture; Kenneth Knoblauch for sharing his R code for the *SLN* fit; Susanne Kunkel for help with creating Fig. 2A; and Helen Barbas and Claus Hilgetag for providing data on neuronal densities and architectural types.

Bibliography

Anderson JC, Kennedy H, Martin KAC. 2011. Pathways of attention: Synaptic relationships of frontal eye field to V4, lateral intraparietal cortex, and area 46 in macaque monkey. J Neurosci. 31:10872–10881.

Angelucci A, Levitt J, Walton E, Hupé J-M, Bullier J, Lund J. 2002. Circuits for local and global signal integration in primary visual cortex. J Neurosci. 22:8633–8646.

Angelucci A, Levitt JB, Lund JS. 2002. Anatomical origins of the classical receptive field and modulatory surround field of single neurons in macaque visual cortical area V1. Prog Brain Res. 136:373–388.

Bakker R, Thomas W, Diesmann M. 2012. CoCoMac 2.0 and the future of tract-tracing databases. Front Neuroinformatics. 6.

Bakker R, Tiesinga P, Kötter R. 2015. The Scalable Brain Atlas: Instant web-based access to public brain atlases and related content. Neuroinformatics. 13:353–366.

Barbas H. 1986. Pattern in the laminar origin of corticocortical connections. Journal of Comparative Neurology. 252:415–422.

Barbas H, Rempel-Clower N. 1997. Cortical structure predicts the pattern of corticocortical connections. Cereb Cortex. 7:635–646.

Barnes CL, Pandya DN. 1992. Efferent cortical connections of multimodal cortex of the superior temporal sulcus in the rhesus monkey. J Compar Neurol. 318:222–244.

Bastos AM, Vezoli J, Bosman CA, Schoffelen J-M, Oostenveld R, Dowdall JR, De Weerd P, Kennedy H, Fries P. 2015. Visual areas exert feedforward and feedback influences through distinct frequency channels. Neuron. 85:390–401.

Beul SF, Barbas H, Hilgetag CC. 2015. A predictive structural model of the primate connectome. arXiv preprint arXiv:151107222. .

Binzegger T, Douglas RJ, Martin KAC. 2004. A quantitative map of the circuit of cat primary visual cortex. J Neurosci. 39:8441–8453.

Bojak I, Oostendorp TF, Reid AT, Kötter R. 2011. Towards a model-based integration of co-registered electroencephalography/functional magnetic resonance imaging data with realistic neural population meshes. Phil Trans R Soc A. 369:3785–3801.

Boussaoud D, Ungerleider L, Desimone R. 1990. Pathways for motion analysis: Cortical connections of the medial superior temporal and fundus of the superior temporal visual areas in the macaque. J Compar Neurol. 296:462–495.

Brunel N. 2000. Dynamics of sparsely connected networks of excitatory and inhibitory spiking neurons. J Comput Neurosci. 8:183–208.

Cabral J, Hugues E, Sporns O, Deco G. 2011. Role of local network oscillations in resting-state functional connectivity. NeuroImage. 57:130–139.

Colby C, Gattass R, Olson C, Gross C. 1988. Topographical organization of cortical afferents to extrastriate visual area PO in the macaque: a dual tracer study. J Compar Neurol. 269:392–413.

Cragg B. 1967. The density of synapses and neurones in the motor and visual areas of the cerebral cortex. J Anat. 101:639–654.

Deco G, Jirsa V, McIntosh AR, Sporns O, Kötter R. 2009. Key role of coupling, delay, and noise in resting brain fluctuations. Proc Natl Acad Sci USA. 106:10302–10307.

Deco G, Jirsa VK. 2012. Ongoing cortical activity at rest: Criticality, multistability, and ghost attractors. J Neurosci. 32:3366–3375.

Distler C, Boussaoud D, Desimone R, Ungerleider LG. 1993. Cortical connections of inferior temporal area teo in macaque monkeys. J Compar Neurol. 334:125–150.

Dombrowski S, Hilgetag C, Barbas H. 2001. Quantitative architecture distinguishes prefrontal cortical systems in the rhesus monkey. Cereb Cortex. 11:975–988.

Eggan S, Lewis D. 2007. Immunocytochemical distribution of the cannabinoid CB1 receptor in the primate neocortex: A regional and laminar analysis. Cereb Cortex. 17:175–191.

Ercsey-Ravasz M, Markov NT, Lamy C, Essen DCV, Knoblauch K, Toroczkai Z, Kennedy H. 2013. A predictive network model of cerebral cortical connectivity based on a distance rule. Neuron. 80:184–197.

Felleman D, Burkhalter A, Van Essen D. 1997. Cortical connections of areas V3 and VP of macaque monkey extrastriate visual cortex. J Compar Neurol. 379:21–47.

Felleman DJ, Van Essen DC. 1991. Distributed hierarchical processing in the primate cerebral cortex. Cereb Cortex. 1:1–47.

Fox MD, Raichle ME. 2007. Spontaneous fluctuations in brain activity observed with functional magnetic resonance imaging. Nature Reviews Neuroscience. 8:700–711.

Fox MD, Snyder AZ, Vincent JL, Corbetta M, Van Essen DC, Raichle ME. 2005. The human brain is intrinsically organized into dynamic, anticorrelated functional networks. Proc Natl Acad Sci USA. 102:9673–9678.

Galletti C, Kutz DF, Gamberini M, Breveglieri R, Fattori P. 2003. Role of the medial parieto-occipital cortex in the control of reaching and grasping movements. Exp Brain Res. 153:158–170.

Gattass R, Sousa A, Mishkin M, Ungerleider L. 1997. Cortical projections of area V2 in the macaque. Cereb Cortex. 7:110–129.

Gewaltig M-O, Diesmann M. 2007. NEST (NEural Simulation Tool). Scholarpedia. 2:1430.

Girard P, Hupé JM, Bullier J. 2001. Feedforward and feedback connections between areas v1 and v2 of the monkey have similar rapid conduction velocities. J Neurophysiol. 85:1328–1331.

Goulas A, Bastiani M, Bezgin G, Uylings HB, Roebroeck A, Stiers P. 2014. Comparative analysis of the macroscale structural connectivity in the macaque and human brain. PLoS Comput Biol. 10:e1003529.

Haeusler S, Schuch K, Maass W. 2009. Motif distribution, dynamical properties, and computational performance of two data-based cortical microcircuit templates. J Physiol (Paris). 103:73–87.

Harrison KH, Hof PR, Wang S-H. 2002. Scaling laws in the mammalian neocortex: Does form provide clues to function? J Neurocytol. 31:289–298.

Hilgetag CC, Medalla M, Beul S, Barbas H. 2015. The primate connectome in context: principles of connections of the cortical visual system. submitted. .

Hill S, Tononi G. 2005. Modeling sleep and wakefulness in the thalamocortical system. J Neurophysiol. 93:1671–1698.

Izhikevich EM, Edelman GM. 2008. Large-scale model of mammalian thalamocortical systems. Proc Natl Acad Sci USA. 105:3593–3598.

Johnson PB, Ferraina S, Bianchi L, Caminiti R. 1996. Cortical networks for visual reaching: physiological and anatomical organization of frontal and parietal lobe arm regions. Cereb Cortex. 6:102–119.

Johnson RR, Burkhalter A. 1996. Microcircuitry of forward and feedback connections within rat visual cortex. J Compar Neurol. 368:383–398.

Johnson RR, Burkhalter A. 1997. A polysynaptic feedback circuit in rat visual cortex. J Neurosci. 17:7129–7140.

Jones E, Coulter J, Hendry S. 1978. Intracortical connectivity of architectonic fields in the somatic sensory, motor and parietal cortex of monkeys. J Compar Neurol. 181:291–347.

Jülich Supercomputing Centre . 2015. JUQUEEN: IBM Blue Gene/Q® supercomputer system at the Jülich Supercomputing Centre. Journal of large-scale research facilities JLSRF. 1:1.

Kandel ER, Markram H, Matthews PM, Yuste R, Koch C. 2013. Neuroscience thinks big (and collaboratively). Nat Rev Neurosci. 14:659–664.

Kunkel S, Schmidt M, Eppler JM, Masumoto G, Igarashi J, Ishii S, Fukai T, Morrison A, Diesmann M, Helias M. 2014. Spiking network simulation code for petascale computers. Front Neuroinformatics. 8:78.

Lamme VA, Super H, Spekreijse H, others . 1998. Feedforward, horizontal, and feedback processing in the visual cortex. Curr Opin Neurobiol. 8:529–535.

Lavenex P, Suzuki W, Amaral D. 2002. Perirhinal and parahippocampal cortices of the macaque monkey: Projections to the neocortex. J Compar Neurol. 447:394–420.

Lesnoff M, Lancelot R. 2012. Analysis of overdispersed data, R package version 13.

Li L, Hu X, Preuss TM, Glasser MF, Damen FW, Qiu Y, Rilling J. 2013. Mapping putative hubs in human, chimpanzee and rhesus macaque connectomes via diffusion tractography. NeuroImage. 80:462–474.

Markov NT, Ercsey-Ravasz MM, Ribeiro Gomes AR, Lamy C, Magrou L, Vezoli J, Misery P, Falchier A, Quilodran R, Gariel MA, Sallet J, Gamanut R, Huissoud C, Clavagnier S, Giroud P, Sappey-Marinier D, Barone P, Dehay C, Toroczkai Z, Knoblauch K, Van Essen DC, Kennedy H. 2014a. A weighted and directed interareal connectivity matrix for macaque cerebral cortex. Cereb Cortex. 24:17–36.

Markov NT, Misery P, Falchier A, Lamy C, Vezoli J, Quilodran R, Gariel MA, Giroud P, Ercsey-Ravasz M, Pilaz LJ, Huissoud C, Barone P, Dehay C, Toroczkai Z, Van Essen DC, Kennedy H, Knoblauch K. 2011. Weight consistency specifies regularities of macaque cortical networks. Cereb Cortex. 21:1254–1272. DOI: 10.1093/cercor/bhq201.

Markov NT, Vezoli J, Chameau P, Falchier A, Quilodran R, Huissoud C, Lamy C, Misery P, Giroud P, Ullman S, Barone P, Dehay C, Knoblauch K, Kennedy H. 2014b. Anatomy of hierarchy: Feedforward and feedback pathways in macaque visual cortex. J Compar Neurol. 522:225–259.

Markram H, Muller E, Ramaswamy S, Reimann MW, Abdellah M, Sanchez CA, Ailamaki A, Alonso-Nanclares L, Antille N, Arsever S, others . 2015. Reconstruction and simulation of neocortical microcircuitry. Cell. 163:456–492.

McCulloch CE, Searle SR, Neuhaus JM. 2008. *Generalized, Linear, and Mixed Models* (2 ed.). Wiley-Interscience.

Morel A, Bullier J. 1990. Anatomical segregation of two cortical visual pathways in the macaque monkey. Visual neuroscience. 4:555–578.

Nordlie E, Gewaltig M-O, Plesser HE. 2009. Towards reproducible descriptions of neuronal network models. PLoS Comput Biol. 5:e1000456.

O'Kusky J, Colonnier M. 1982. A laminar analysis of the number of neurons, glia, and synapses in the visual cortex (area 17) of adult macaque monkeys. J Compar Neurol. 210:278–290.

Pascual-Leone A, Walsh V. 2001. Fast backprojections from the motion to the primary visual area necessary for visual awareness. Science. 292:510–512.

Perkel DJ, Bullier J, Kennedy H. 1986. Topography of the afferent connectivity of area 17 in the macaque monkey: A double-labelling study. J Compar Neurol. 253:374–402.

Petrides M, Pandya D. 1999. Dorsolateral prefrontal cortex: comparative cytoarchitectonic analysis in the human and the macaque brain and corticocortical connection patterns. Eur J Neurosci. 11:1011–1036.

Potjans TC, Diesmann M. 2013. Multi-population network models of the cortical microcircuit. In *Advances in Cognitive Neurodynamics (III)*, pp. 91–96. Springer.

Potjans TC, Diesmann M. 2014. The cell-type specific cortical microcircuit: Relating structure and activity in a full-scale spiking network model. Cereb Cortex. 24:785–806. doi: 10.1093/cercor/bhs358.

Preissl R, Wong TM, Datta P, Flickner M, Singh R, Esser SK, Risk WP, Simon HD, Modha DS. 2012. Compass: a scalable simulator for an architecture for Cognitive Computing. In *Proceedings of the International Conference on High Performance Computing, Networking, Storage and Analysis*, SC '12, Los Alamitos, CA, USA, pp. 54:1–54:11. IEEE Computer Society Press.

Preuss T, Goldman-Rakic P. 1991. Architectonics of the parietal and temporal association cortex in the strepsirhine primate galago compared to the anthropoid primate macaca. J Compar Neurol. 310:475–506.

R Core Team . 2015. *R: A Language and Environment for Statistical Computing*. Vienna, Austria: R Foundation for Statistical Computing.

Rakic P, Suñer I, Williams R. 1991. A novel cytoarchitectonic area induced experimentally within the primate visual cortex. Proc Nat Acad Sci USA. 88:2083–2087.

Rao RPN, Ballard DH. 1999. Predictive coding in the visual cortex: a functional interpretation of some extra-classical receptive field effects. Nat Neurosci. 2:79–87.

Rasch MJ, Schuch K, Logothetis NK, Maass W. 2011. Statistical comparison of spike responses to natural stimuli in monkey area V1 with simulated responses of a detailed laminar network model for a patch of V1. J Neurophysiol. 105:757–778.

Riesenhuber M, Poggio T. 1999. Hierarchical models of object recognition in cortex. Nat Neurosci. 2:1019–1025.

RIKEN BSI . 2013. Largest neuronal network simulation achieved using K computer. Press release.

Rockland K. 1992. Configuration, in serial reconstruction, of individual axons projecting from area V2 to V4 in the macaque monkey. Cereb Cortex. 2:353–374.

Rockland KS, Andresen J, Cowie RJ, Robinson DL. 1999. Single axon analysis of pulvinocortical connections to several visual areas in the macaque. Journal of Comparative Neurology. 406:221–250.

Rockland KS, Pandya DN. 1979. Laminar origins and terminations of cortical connections of the occipital lobe in the rhesus monkey. Brain Res. 179:3–20.

Rozzi S, Calzavara R, Belmalih A, Borra E, Gregoriou G, Matelli M, Luppino G. 2006. Cortical connections of the inferior parietal cortical convexity of the macaque monkey. Cereb Cortex. 16:1389–1417.

Sakata S, Harris KD. 2009. Laminar structure of spontaneous and sensory-evoked population activity in auditory cortex. Neuron. 64:404–418.

Salin P, Bullier J, Kennedy H. 1989. Convergence and divergence in the afferent projections to cat area 17. J Compar Neurol. 283:486–512.

Salin P-A, Bullier J. 1995. Corticocortical connections in the visual system: structure and function. Physiol Rev. 75:107–154.

Schmidt M, van Albada S, Bakker R, Diesmann M. 2013. Integrating multi-scale data for a network model of macaque visual cortex. BMC Neuroscience. 14(Suppl 1):P111.

Schmidt M, van Albada S, Bakker R, Diesmann M. 2014. A spiking multi-area network model of macaque visual cortex. In *2014 Neuroscience Meeting Planner. Washington, DC: Society for Neuroscience.*, pp. 186.22/TT43.

Schroeder CE, Mehta AD, Givre SJ. 1998. A spatiotemporal profile of visual system activation revealed by current source density analysis in the awake macaque. Cereb Cortex. 8:575–592.

Schuecker J, Schmidt M, van Albada S, Diesmann M, Helias M. 2015. Fundamental activity constraints lead to specific interpretations of the connectome. arXiv preprint arXiv:150903162. .

Schüz A, Palm G. 1989. Density of neurons and synapses in the cerebral cortex of the mouse. J Compar Neurol. 286:442–455.

Seltzer B, Pandya DN. 1994. Parietal, temporal, and occipita projections to cortex of the superior temporal sulcus in the rhesus monkey: A retrograde tracer study. J Compar Neurol. 343:445–463.

Shen K, Bezgin G, Hutchison R, Gati J, Menon R, Everling S, McIntosh R. 2012. Information processing architecture of functionally defined clusters in the macaque cortex. J Neurosci. 32:17465–17476.

Shen K, Hutchison RM, Bezgin G, Everling S, McIntosh AR. 2015. Network structure shapes spontaneous functional connectivity dynamics. J Neurosci. 35:5579–5588.

Sheng T. 1985. The distance between two random points in plane regions. Adv Appl Prob. 17:748–773.

Stephan K, Kamper L, Bozkurt A, Burns G, Young M, Kötter R. 2001. Advanced database methodology for the collation of connectivity data on the macaque brain (CoCoMac). Phil Trans R Soc B. 356:1159–1186.

Suzuki WA, Amaral DG. 1994a. Topographic organization of the reciprocal connections between the monkey entorhinal cortex and the perirhinal and parahippocampal cortices. J Neurosci. 14:1856–1877.

Suzuki WL, Amaral DG. 1994b. Perirhinal and parahippocampal cortices of the macaque monkey: cortical afferents. J Compar Neurol. 350:497–533.

Thomas C, Frank QY, Irfanoglu MO, Modi P, Saleem KS, Leopold DA, Pierpaoli C. 2014. Anatomical accuracy of brain connections derived from diffusion mri tractography is inherently limited. Proc Natl Acad Sci USA. 111:16574–16579.

Thomson AM, Lamy C. 2007. Functional maps of neocortical local circuitry. Front Neurosci. 1:19–42.

Tiesinga P, Bakker R, Hill S, Bjaalie JG. 2015. Feeding the human brain model. Curr Opin Neurobiol. 32:107–114.

Tomioka R, Rockland KS. 2007. Long-distance corticocortical GABAergic neurons in the adult monkey white and gray matter. J Compar Neurol. 505:526–538.

Traub RD, Contreras D, Cunningham MO, Murray H, LeBeau FEN, Roopun A, Bibbig A, Wilent WB, Higley MJ, Whittington MA. 2005. Single-column thalamocortical network model exhibiting gamma oscillations, sleep spindles, and epileptogenic bursts. J Neurophysiol. 93:2194–2232.

van Albada SJ, Helias M, Diesmann M. 2015. Scalability of asynchronous networks is limited by one-to-one mapping between effective connectivity and correlations. PLoS Comput Biol. 11:e1004490.

Van Essen DC. 2002. Windows on the brain: the emerging role of atlases and databases in neuroscience. Curr Opin Neurobiol. 12:574–579.

Van Essen DC, Drury HA, Dickson J, Harwell J, Hanlon D, Anderson CH. 2001. An integrated software suite for surface-based analyses of cerebral cortex. Journal of the American Medical Informatics Association. 8:443–459.

Voges N, Perrinet LU. 2012. Complex dynamics in recurrent cortical networks based on spatially realistic connectivities. Front Comput Neurosci. 6:41.

Wagstyl K, Ronan L, Goodyer IM, Fletcher PC. 2015. Cortical thickness gradients in structural hierarchies. NeuroImage. 111:241–250.

Webster M, Ungerleider L, Bachevalier J. 1991. Connections of inferior temporal areas TE and TEO with medial temporal-lobe structures in infant and adult monkeys. J Neurosci. 11:1095–1116.

Webster MJ, Bachevalier J, Ungerleider LG. 1994. Connections of inferior temporal areas TEO and TE with parietal and frontal cortex in macaque monkeys. Cereb Cortex. 4:470–483.

Weisstein EW. 2005. Beta binomial distribution. From MathWorld–A Wolfram Web Resource. .

Supplement

Neuron and synapse parameters

Synapse parameters		
Name	**Value**	**Description**
$w \pm \delta w$	V1: 87.8 ± 8.8 pA, either equal for other areas or scaled as $w \propto \rho(A)^\kappa$, $\kappa \in [0, 1]$	excitatory synaptic strength
g	variable, $g \in [-10, -4]$	relative inhibitory synaptic strength
$d_\mathrm{e} \pm \delta d_\mathrm{e}$	1.5 ± 0.75 ms	local excitatory transmission delay
$d_\mathrm{i} \pm \delta d_\mathrm{i}$	0.75 ± 0.375 ms	local inhibitory transmission delay
$d \pm \delta d$	$s/v_\mathrm{t} \pm \frac{1}{2} s/v_\mathrm{t}$	inter-areal transmission delay, with s the distance between areas
v_t	3.5 m/s	transmission speed
Neuron model		
Name	**Value**	**Description**
τ_m	10 ms	membrane time constant
τ_r	2 ms	absolute refractory period
τ_s	0.5 ms	postsynaptic current time constant
C_m	250 pF	membrane capacity
V_r	-65 mV	reset potential
θ	-50 mV	fixed firing threshold
E_L	-65 mV	leak potential

Table S1: Parameter specification for single synapses and neurons.

Translation of architectural types

Area in Hilgetag et al. (2015)	**FV91 area**	**Area in** Hilgetag et al. (2015)	**FV91 area**
V1	V1	MST	MSTd, MSTl
V2	V2	PIP	PIP
V3	V3	PIT	PITd, PITv
VP	VP	PO	PO
MT	MT	TF	TF
V3A	V3A	VIP	VIP
V4	V4	A46v	46
V4t	V4t	A7a	7a
VOT	VOT	AIT	AITd, AITv
CIT	CITd, CITv	FST	FST
DP	DP	STP	STPa, STPp
FEF	FEF	TH	TH
LIPd, LIPv	LIP		

Table S2: Scheme for translating areas given in Table 4 of Hilgetag et al. (2015) to the modeled areas in the parcellation scheme of Felleman & Van Essen (1991).

Area surfaces

Area	Surface area (mm^2)	Area	Surface area (mm^2)	Area	Surface area (mm^2)
V1	1484.63	V3	120.57	PO	75.37
V2	1193.40	CITv	114.67	VOT	70.11
V4	561.41	DP	113.83	LIP	56.04
STPp	245.48	PIP	106.15	MT	55.90
TF	197.40	PITv	100.34	FST	61.33
46	185.16	AITd	91.59	CITd	57.54
FEF	161.54	VIP	85.06	MIP	45.09
7a	157.34	V3A	96.96	TH	44.60
PITd	145.38	AITv	93.12	MSTl	29.19
VP	130.58	STPa	78.72	V4t	28.23
MSTd	120.57	MDP	77.49		

Table S3: Surface areas computed with Caret (Van Essen et al., 2001) on the basis of each area's representation on the F99 cortical surface (Van Essen, 2002). Areas are ordered from large to small.

Processing of CoCoMac data

The CoCoMac database provides information on laminar patterns on the source side from retrograde tracing studies as well as on the target side from anterograde tracing studies. The data was extracted by using the following link, which specifies all search options:

`http://cocomac.g-node.org/cocomac2/services/connectivity_matrix.php?dbdate=20141022&AP=AxonalProjections_FV91&constraint=&origins=&terminals=&square=1&merge=max&laminar=both&format=json&cite=1`

Furthermore, we obtained the numbers of confirmative studies for each area-level connection with the following link:

`http://cocomac.g-node.org/cocomac2/services/connectivity_matrix.php?dbdate=20141022&AP=AxonalProjections_FV91&constraint=&origins=&terminals=&square=1&merge=count&laminar=off&format=json&cite=1`

To process these data, we applied the following steps:

- A connection is assumed to exist if there is at least one confirmative study reporting it.
- A connection from layer 2/3 is modeled if CoCoMac indicates a connection from either or both of layers 2 and 3.
- In the database, some layers carry an 'X' indicating a connection of unknown strength. We interpret these as '2' (corresponding to medium connection strength).

Mapping of injection sites to FV91 parcellation

Monkey	M132 area	FV91 area	Monkey	M132 area	FV91 area
M88RH	V1	V1	M101LH	V2	V2
M121LH	V1	V1	M101RH	V2	V2
M81LH	V1	V1	M103LH	V2	V2
M85LH	V1	V1	M123LH	V4	V4
M85RH	V1	V1	M121RH	V4	V4
BB289RH	STPr	STPa	M119LH	TEO	V4
BB289LH	STPi	STPp	BB135LH	7A	7a
M90RH	STPc	STPp	M89LH	DP	DP
M106LH	9/46d	FEF	BB272RH	8l	FEF
M133LH	MT	MSTd	M116LH	46d	46
M116RH	9/46v	46	BB272LH	8m	FEF
M128RH	TEPd	CITv	M108LH	PBr	STPp

Table S4: Injected areas of the data set of Markov et al. (2014a) in the M132 parcellation and corresponding areas in the FV91 scheme. Only the injections in vision-related cortex are shown.

Mapping of synapse to cell-body locations

Detailed calculation in section "Construction of the model". The numbers are listed in Table S5.

		Synapse layer				
		1	**2/3**	**4**	**5**	**6**
Target population	2/3E	0.57				
	2/3I		0.16			
	4E	0.18	0.84	0.73		
	4I			0.16		
	5E	0.25		0.02	0.76	
	5I				0.1	
	6E	0.003		0.09	0.14	0.85
	6I					0.15

Table S5: Conditional probabilities $\mathcal{P}(i|s_{\mathrm{cc}} \in v)$ for the target neuron to belong to population i if a cortico-cortical synapse s_{cc} is located in layer v, computed with (11) applied to the data set of Binzegger et al. (2004). Empty cells signal zero probabilities.

Connection probabilities

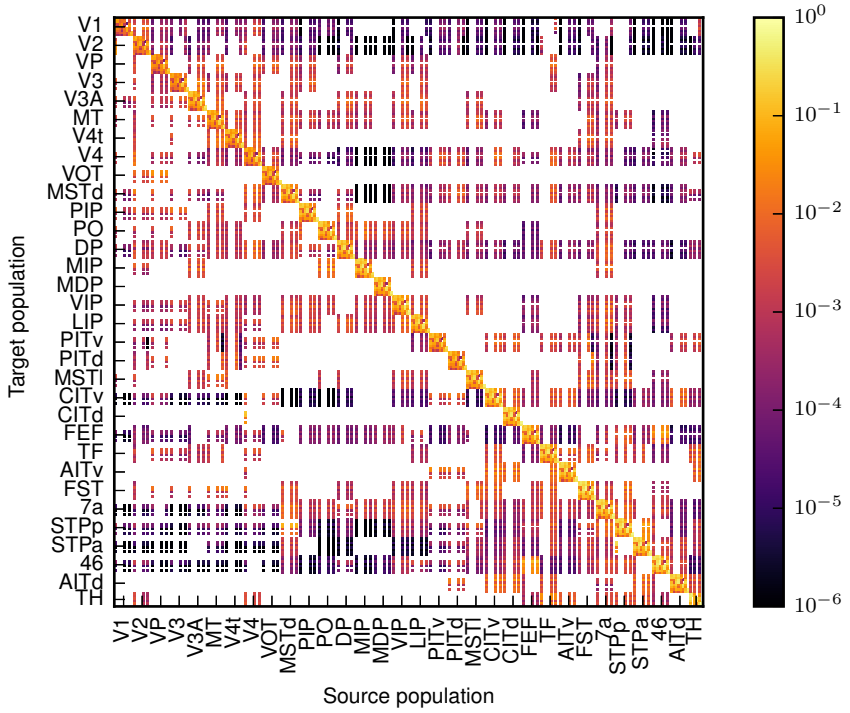

Figure S1: Connection probabilities of the model encoded in color. Areas are ordered according to their architectural types, and populations inside the areas are ordered as [2/3E, 2/3I, 4E/, 4I, 5E, 5I, 6E, 6I].